https://dx.doi.org/10.1016/j.buildenv.2022.108823

Generalizability evaluation of k-ε models calibrated by using Ensemble Kalman filtering for urban airflow and airborne contaminant dispersion

Runmin Zhao[a], Sumei Liu[a*], Junjie Liu[a], Nan Jiang[b], Qingyan Chen[c]

[a]*Tianjin Key Laboratory of Indoor Air Environmental Quality Control, School of Environmental Science and Engineering, Tianjin University, Tianjin 300072, China*

[b]*School of Mechanical Engineering, Tianjin University, Tianjin 300072, China*

[c] *Department of Building Environment and Energy Engineering, The Hong Kong Polytechnic University, Kowloon, 999077, Hong Kong SAR, China*

** Corresponding author's email address: smliu@tju.edu.cn (Sumei Liu)*

E-mail addresses: zhaorm@tju.edu.cn (Runmin Zhao), jjliu@tju.edu.cn (Junjie Liu), nanj@tju.edu.cn (Nan Jiang); yanchen@purdue.edu (Qingyan Chen)

HIGHLIGHTS

- Employment of EnKF to calibrate model coefficients for urban problems.
- Main calibrations based on reattachment lengths for improved accuracy.
- Model generalizability found to be closely related to model formulations.
- Potential generalizability of the calibrated MMK to single-building problems.
- Limited generalizability from isolated roughness flow to skimming flow.

Abstract

The low accuracy of Reynolds-averaged Navier-Stokes (RANS) modeling of urban airflow and airborne pollutant dispersion is attributed to model flaws and uncertainty contributed by closure coefficients. Previous studies have attempted to improve the performance of RANS modeling by ad hoc calibration of the turbulence model coefficients specifically for urban problems. However, these models failed to accurately reproduce the key features like the reattachment lengths. In addition, there was a lack of generalizability evaluations of the calibrated models. To optimize the accuracy and generalizability of those turbulence model, this study considered the effects of optimization objectives and model formulations. Six *k*-ε based turbulence models calibrated using the ensemble Kalman filtering (EnKF) approach were compared. A wind tunnel experiment consisting of key features of the airflow around a single-building model was conducted to provide the training data. The proposed optimization objective prioritizing the reproduction of the reattachment lengths in the calibrations enabled the calibrated models to capture the key features of the airflow with better accuracy. The six turbulence models before and after the calibrations were compared for a single-building test case and a building-array test case with respect to the reattachment lengths, velocity, turbulence kinetic energy, and airborne contaminant concentration. The calibrated models with different formulations exhibit distinctive generalizability. The calibrated Murakami-Mochida-Kondo *k*-ε model (MMK) exhibited strong potential for generalizability to single-building problems. However, the generalization from the single-building isolated roughness flow regime to the street canyon skimming flow regime is limited.

Keywords: Computational fluid dynamics, Turbulence model, Urban airflow, Pollutant dispersion, Ensemble Kalman filtering

1 Introduction

Urban airflow and pollutant dispersion around buildings are important environmental problems [1]. High wind speeds introduced at the pedestrian level by high-rise buildings can cause wind nuisance and safety issues [2]. High concentrations of pollutants emitted by vehicles and from building exhausts harm pedestrian health and contaminate indoor air through building intakes [3]. Therefore, it is essential to investigate airflow and pollutant dispersion around buildings.

Studies of the airflow field and pollutant distributions around buildings often use field measurements [4–7] and reduced-scale wind tunnel experiments [8]. However, experimental studies are very expensive and have often been limited to typical cases. Meanwhile, computational fluid dynamics (CFD) has been extensively employed in urban studies in recent decades [9]. The two most popular CFD approaches are large-eddy simulation (LES) and Reynolds-averaged Navier-Stokes (RANS) modeling. LES resolves large-scale turbulence with high spatial and temporal resolution and exhibits better agreement with experimental data than RANS [10], but LES is computationally demanding, especially when the full scale of urban problems is considered [11]. Most wind engineering applications still employ steady Reynolds-averaged Navier-Stokes (SRANS) modeling as the main workhorse because of its computational efficiency and readily available guidelines [12–16]. However, commonly

58 employed two-equation turbulence models have known issues in urban problems, such as the
59 overprediction of velocity in weak wind regions around buildings, inaccurate prediction of
60 reattachment lengths, and underprediction of turbulence kinetic energy [17–21]. The low
61 accuracy of two-equation models can be attributed mainly to the Boussinesq hypothesis and
62 the uncertainties contributed by empirical formulations and closure coefficients. Various
63 modifications to the two-equation models may fix certain flaws. Advanced techniques like data
64 assimilation and machine learning can also improve the performance of RANS modeling [22].
65 However, employing these advanced frameworks in practical usages often requires user
66 expertise and sometimes extra computing resources [23].
67 Another approach to improve the performance of RANS modeling is the calibration of the
68 closure coefficients in the turbulence models. Once calibrated, the coefficients can be readily
69 employed in engineering applications. Several attempts have been made to calibrate the
70 coefficients of the models specifically for urban problems. The calibrated models include the
71 standard k-ε model (SKE) [24–26], Kato-Launder k-ε model (KL) [27,28], Durbin k-ε model
72 (DKE) [29], Re-Normalisation Group k-ε model (RNG), and Spalart–Allmaras model [30]. The
73 consensus was that a case-specific calibration of model coefficients would allow wind tunnel
74 data to be reconstructed with greater accuracy. However, the calibrated models can still fail to
75 accurately reproduce the key features like the reattachment lengths. For example, the calibrated
76 k-ε models in Shirzadi et al. [27] and Shirzadi et al. [28] still overpredicted the reattachment
77 lengths behind the isolated building by around 30%. The exaggerated recirculation zone would
78 contribute to wrong results in dispersion modeling, which is one of the main topics in urban

studies but has not been tested for the calibrated models. One possible way to mitigate this overprediction is to adjust the optimization objective by including the key features of the airflow. However, there were not many wind tunnel experiments reporting the reattachment lengths both on the roof and behind the building. In addition, previous studies did not conduct generalizability tests for the calibrated models. As pointed out by some researchers, the inherent shortcomings of the RANS-based turbulence models cannot be eliminated simply by tuning the model coefficients [25,27,28]. As a result, a bespoke calibration suitable for one scenario may bring adverse effects to another scenario, which hinders the application of the calibrated models. The model generalizability might be related to the model formulations, calling for comprehensive model comparisons. Previous studies employed different methods to reduce the complexity of the optimization problem. Two of the studies [26,29] adjusted only a few key coefficients out of the whole set, while other studies [24,25,27,28] reduced the unknowns by using the empirical relationship between the model coefficients in the atmospheric boundary layer (ABL) flow described by Richards and Hoxey [31], which only holds for the standard k-ε model, strictly speaking. For different model variants with many coefficients, a calibration of the whole set of model coefficients is necessary. The increased complexity of the problem requires a robust optimization method. The ensemble Kalman filtering (EnKF) approach has been used successfully in the calibration of closure coefficients for the Spalart–Allmaras model [32], k-ω SST model [33], and k-ω-γ-A_r four-equation model [34] for different flow problems. However, this method has not yet been employed to calibrate turbulence models specifically for urban problems.

Previous investigations failed to accurately reproduce the key features like the reattachment lengths. They did not conduct generalizability tests for the calibrated models. This investigation used a wind tunnel experiment to obtain the velocity field around an isolated low-rise building as well as the reattachment lengths both on the roof and behind the building. The EnKF approach was used to optimize the accuracy of k-ε models by including the key features of the airflow. The generalizability of the obtained turbulence model was further evaluated by employing two test cases featuring different flow regimes.

2 Methods

This section describes the main methods used for model coefficient calibration. The chosen k-ε based models for calibration are introduced in Subsection 2.1. The calibration was based on an EnKF loop (see Subsection 2.2), which iteratively updated the model coefficients determined from the discrepancy between CFD results and observation data from a wind tunnel experiment (see Subsection 2.3). The validity of each calibrated model was assessed according to the metrics introduced in Subsection 2.4. The framework of the calibration methods is provided in Fig.1.

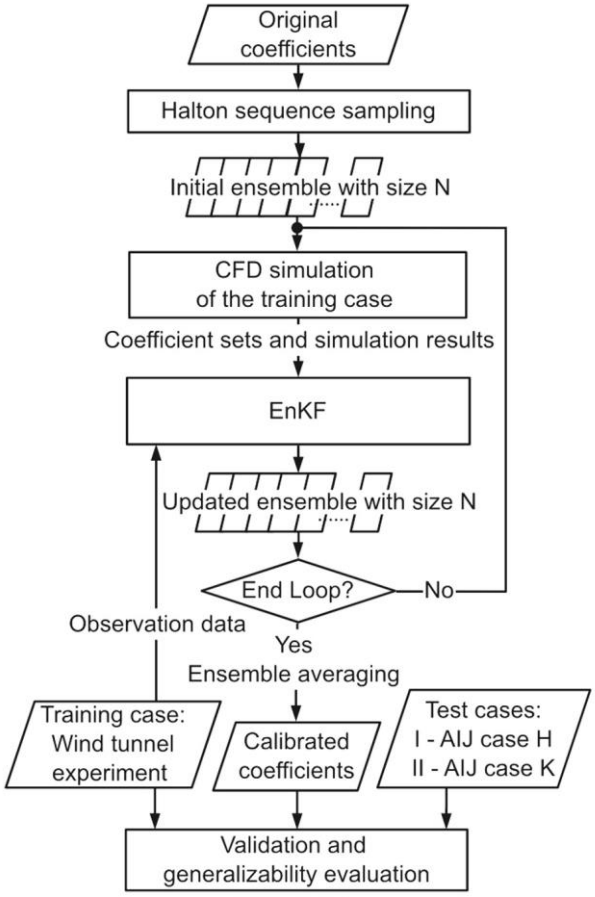

Figure 1 Framework of the calibration methods. The calibration was based on an EnKF loop that iteratively updated the model coefficients determined from the discrepancy between CFD results and observation data from a wind tunnel experiment.

2.1 Governing equations and turbulence modeling

This subsection describes the governing equations and the turbulence models chosen for calibration. The steady-state incompressible RANS equations in conservation form, without considering body forces, can be written in Einstein notation as

$$\frac{\partial U_i}{\partial x_i}=0, \tag{1}$$

$$\frac{\partial\left(U_j U_i\right)}{\partial x_j}=-\frac{1}{\rho}\frac{\partial \overline{p}}{\partial x_i}+\frac{\partial}{\partial x_j}\left(\nu\frac{\partial U_i}{\partial x_j}-\overline{u_i' u_j'}\right), \tag{2}$$

where U_i, U_j are the mean velocity components, u_i', u_j' are the fluctuating velocity components in the x_i, x_j directions (i, j = 1, 2, 3). p is the pressure, ν is the kinematic viscosity, and ρ is the density.

A prescription is needed for computing $-\overline{u_i'u_j'}$ for the calculation of all mean-flow properties. Assuming that the Boussinesq linear isotropic eddy-viscosity hypothesis is valid, the specific Reynolds-stress tensor is expressed by

$$-\overline{u_i'u_j'}=2\nu_t S_{ij}-\frac{2}{3}k\delta_{ij}, \tag{3}$$

where ν_t is the kinematic eddy viscosity, $k = \frac{1}{2}\overline{u_i'u_i'}$ is the turbulence kinetic energy (TKE), $S_{ij}=(\partial U_j/\partial x_i+\partial U_i/\partial x_j)/2$ is the strain rate tensor, and δ_{ij} is the Kronecker Delta function. In this study, the k-ε two-equation model was chosen to close the equation system. The transport equation for k and the turbulence dissipation rate ε are

$$\frac{\partial(U_j k)}{\partial x_j}=\frac{\partial}{\partial x_j}\left[\left(\nu+\frac{\nu_t}{\sigma_k}\right)\frac{\partial k}{\partial x_j}\right]+P_k-\varepsilon, \tag{4}$$

and

$$\frac{\partial(U_j \varepsilon)}{\partial x_j}=\frac{\partial}{\partial x_j}\left[\left(\nu+\frac{\nu_t}{\sigma_\varepsilon}\right)\frac{\partial \varepsilon}{\partial x_j}\right]+S_\varepsilon\ , \tag{5}$$

where P_k is the production term, ε is the turbulence dissipation rate, and S_ε is the source term. Variants of the k-ε model differ mainly in the calculation of ν_t, P_k and S_ε. This study chose the most popular k-ε models in urban studies for comparison [35,36]. Table 1 outlines the formulations of the six chosen k-ε based models without considering the buoyancy effect, including the standard k-ε model (SKE) and five variants featuring modifications related to overproduction of TKE (KL, MMK, and DKE), spreading rate (Realizable k-ε, denoted RKE),

and small scales of motion (RNG). The standard values of the model coefficients listed in Table 1 were initially determined by ensuring agreement with observations in fundamental flow phenomena such as decaying homogeneous isotropic turbulence, channel flow, simple shear, and pure extension [37]. These 'standard' coefficient sets may not be suitable for commonly encountered issues such as airflow around buildings featuring impingement, separation, and vortex shedding [38], and therefore they should be calibrated for better application in urban problems. Unlike some previous studies which focused on only a few key coefficients instead of the whole set [26,29] or reduced the unknowns using empirical formulae [24,25,27,28], the present study calibrated all the listed coefficients for each turbulence model.

Table 1 Formulations and model coefficients of the turbulence models. The chosen models were the most frequently used k-ε models in urban studies.

Turbulence model	ν_t	P_k	S_ε	Coefficients
Standard k-ε (SKE) [39]	$C_\mu \frac{k^2}{\varepsilon}$	$\nu_t S^2$, $S=\sqrt{2S_{ij}S_{ij}}$,	$C_{\varepsilon1}\frac{\varepsilon}{k}P_k - C_{\varepsilon2}\frac{\varepsilon^2}{k}$	C_μ, $C_{\varepsilon1}$, $C_{\varepsilon2}$, σ_k, σ_ε
Kato-Launder k-ε (KL) [40]		$\nu_t S\Omega$, $\Omega=\sqrt{2\Omega_{ij}\Omega_{ij}}$, $\Omega_{ij}=\frac{1}{2}\left(\frac{\partial U_j}{\partial x_i}-\frac{\partial U_i}{\partial x_j}\right)$		
Murakami-Mochida-Kondo k-ε (MMK) [41]	$C_\mu \frac{k^2}{\varepsilon}$ ($\Omega/S\geq1$), $C_\mu \frac{k^2}{\varepsilon}\frac{\Omega}{S}$ ($\Omega/S<1$)	$\nu_t S^2$		
Durbin k-ε (DKE) [42]	$C_\mu Tk$, $T=\min\left(\frac{k}{\varepsilon}, \alpha\frac{1}{\sqrt{3}}\frac{1}{C_\mu S}\right)$.		$C_{\varepsilon1}\frac{1}{T}P_k - C_{\varepsilon2}\frac{\varepsilon}{T}$	C_μ, $C_{\varepsilon1}$, $C_{\varepsilon2}$, σ_k, σ_ε, α
Realizable k-ε (RKE) [43]	$C_\mu \frac{k^2}{\varepsilon}$, $C_\mu=\frac{1}{A_0+A_s\frac{kU^*}{\varepsilon}}$. (See Shin et al. [43] for detailed formulations for A_s and U^*)		$C_1 S\varepsilon - C_{\varepsilon2}\frac{\varepsilon^2}{k+\sqrt{\nu\varepsilon}}$, $C_1=\max\left[0.43, \frac{\eta}{\eta+5}\right]$, $\eta=S\frac{k}{\varepsilon}$.	A_0, $C_{\varepsilon2}$, σ_k, σ_ε

Re-Normalisation Group k-ε (RNG) [44]	$C_\mu \frac{k^2}{\varepsilon}$		$C_{\varepsilon 1}\frac{\varepsilon}{k}P_k - C_{2\varepsilon}^*\frac{\varepsilon^2}{k}$, $C_{2\varepsilon}^* = C_{2\varepsilon} + \frac{C_\mu \eta^3 (1-\eta/\eta_0)}{1+\beta\eta^3}$,	C_μ, $C_{\varepsilon 1}$, $C_{\varepsilon 2}$, σ_k, σ_ε, β, η_0

149

150 The gas dispersion is modeled by a convection-diffusion equation:

$$\frac{\partial (U_j C)}{\partial x_j} = \frac{\partial}{\partial x_j}\left[\left(\frac{\nu}{Sc} + \frac{\nu_t}{Sc_t}\right)\frac{\partial C}{\partial x_j}\right], \tag{6}$$

151 where C is the concentration, Sc is the Schmidt number, and Sc_t is the turbulent Schmidt

152 number.

153 2.2 EnKF for model coefficient calibration

154 To fine-tune the model coefficients introduced in the above subsection, a calibration framework

155 was needed. This subsection provides a brief description of the optimization problem in the

156 calibration process and the EnKF approach to solve it.

157 The model coefficient calibration is based on an inverse problem aimed at finding the

158 coefficient set $\boldsymbol{x}^{opt}$ that leads to the CFD result that agrees most closely with the chosen

159 observation $\boldsymbol{y}$, which can be constructed with point data for measured quantities or key

160 parameters such as the reattachment lengths. The inverse problem can be written as

$$\boldsymbol{x}^{opt} = \text{argmin } J, \text{ with } J(\boldsymbol{x}) = \|\boldsymbol{H}(\boldsymbol{x}) - \boldsymbol{y}\|^2, \tag{7}$$

161 Where argmin means the argument of minimum, J is the cost function, and $\boldsymbol{H}$ is the forward

162 operator which represents the mapping from the coefficient set space to the observation space

163 by the CFD simulation.

From a Bayesian point of view, the solution of the inverse problem equates to finding the posterior distribution $P(\boldsymbol{x}|\boldsymbol{y})$ by combining the data distribution $P(\boldsymbol{y}|\boldsymbol{x})$ and the prior distribution $P(\boldsymbol{x})$ and can be written as

$$P(\boldsymbol{x}|\boldsymbol{y}) \propto P(\boldsymbol{y}|\boldsymbol{x})P(\boldsymbol{x}). \tag{8}$$

In this form, the inverse problem can be solved with the use of the EnKF approach. EnKF was first introduced by Evensen [45] and was employed extensively in data assimilation studies. Iglesias et al. [46] proposed the application of EnKF as a derivative-free optimizer for solving inverse problems. The method is simple in its conceptual formulation and easy to implement. A brief description is provided below.

EnKF is an ensemble method, which means that the prior statistics are represented by an ensemble $\{\boldsymbol{x}_k^{(j)}\}_{j=1}^{N}$ in the kth step, where N is the ensemble size. In this study, each ensemble is a collection of N coefficient sets, which are updated iteratively. Each sample $\boldsymbol{x}_k^{(j)}$ is updated as

$$\boldsymbol{x}_{k+1}^{(j)}=\boldsymbol{x}_k^{(j)}+\boldsymbol{K}(\boldsymbol{y} - \boldsymbol{H}(\boldsymbol{x}_k^{(j)})), \tag{9}$$

where $\boldsymbol{K}$ is the Kalman gain matrix and calculated as

$$\boldsymbol{K} = \boldsymbol{P}\boldsymbol{H}^T(\boldsymbol{H}\boldsymbol{P}\boldsymbol{H}^T+\boldsymbol{\Gamma})^{-1}. \tag{10}$$

Here, $\boldsymbol{P}$ is the covariance of the ensemble and $\boldsymbol{\Gamma}$ is the observation covariance error, which can be determined from the variations of the measured quantities from repeated experiments.

The main loop of the EnKF calibration procedure can be summarized as follows:

1. Prepare the initial ensemble $\{\boldsymbol{x}_0^{(j)}\}_{j=1}^{N}$ around the default coefficient set $\boldsymbol{x}_0$ with the use of a sampling technique;

2. For each ensemble member, solve the RANS equation to map the coefficient set to the observation space and obtain $\boldsymbol{H}$ for the step;

3. Calculate the Kalman gain matrix $\boldsymbol{K}$ according to Eq. (10) and update the ensemble based on Eq. (9);

4. Return to Step 2 until further minimization of the discrepancy cannot be achieved; and

5. Output the ensemble average as the calibrated coefficient set.

2.3 Wind tunnel experiment

The observation data introduced in the above subsection is often obtained from wind tunnel experiments. Previous studies mainly used point data for various flow quantities as observations. However, as mentioned in Section 1, it is meaningful to include the key features of the airflow like the reattachment lengths in the optimization objectives. Since this study included both calibration and generalizability tests, two datasets reporting the reattachment lengths were needed. Wind tunnel experiments reporting the reattachment lengths both on the roof and behind the building were scarce. Therefore, a wind tunnel experiment was conducted to obtain the velocity field and the reattachment lengths.

The wind tunnel experiment was carried out in an open-circuit wind tunnel at Tianjin University. The cross-section at which the measurements took place had effective dimensions of 0.35 m in width × 0.225 m in height. A set of four triangular spires, designed in accordance with Irwin's approach [47], were mounted in the extreme upstream region. Seven thin bars were attached horizontally to the spires to maintain the necessary turbulence intensity, with inspiration from the lattice method for part-depth ABL flow simulation in wind tunnels [48].

A roughness-element fetch was arranged downwind of the spires with cubes of decreasing heights. After continuous adjustments to the spacings between the bars and the layout of the roughness elements, an ABL flow profile was achieved. The vertical profile of the mean wind velocity followed a 0.25 power law (Eq. 11). The profile of the streamwise turbulence intensity I_x followed the empirical equation (Eq. 12) suggested by the American Society of Civil Engineers (ASCE) [49]. In Eq. 12, $\sigma_U(z)$ is the standard deviation of the measured velocity, and the regional roughness height $z_0 = 1.8\times10^{-4}$ m. Despite several measured values of I_x far from the theoretical curve in the upper region, relaxing the requirement for I_x would not affect the validation study since it is a common practice to prescribe the measured values, instead of the theoretical profiles of the ABL, as the boundary conditions. Fig. 2 shows the measured velocity and turbulence intensity profiles of the incident flow.

$$\frac{U(z)}{U_H} = \left(\frac{z}{H}\right)^{0.25} \tag{11}$$

$$I_x(z) = \frac{\sigma_U(z)}{U(z)} = \frac{1}{\ln(z/z_0)} \tag{12}$$

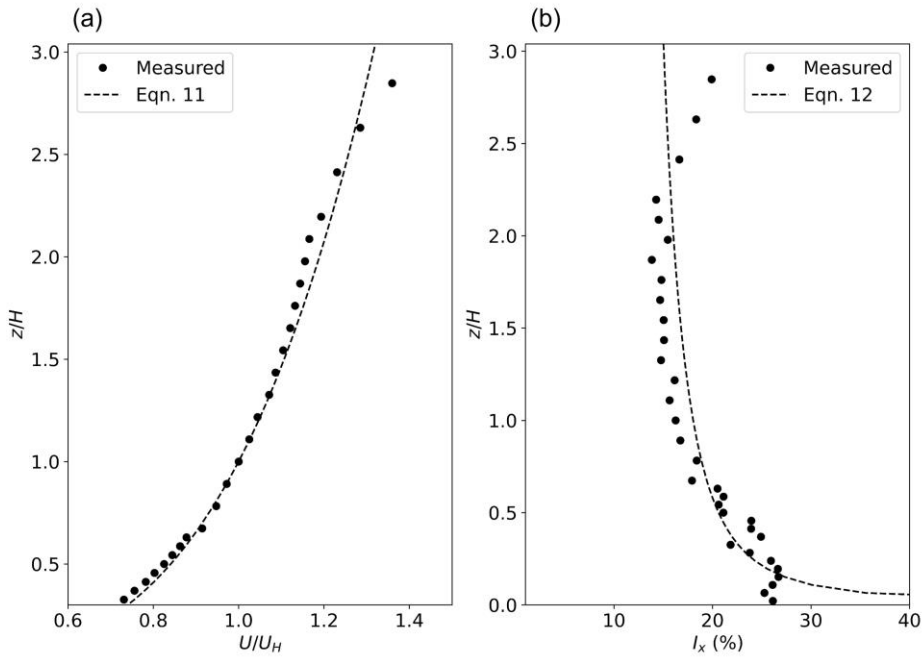

Figure 2 Profiles of (a) velocity and (b) turbulence intensity of the formulated ABL flow for the wind-tunnel experiment, which provides the training data for the calibration. The formulated velocity profile follows a 0.25 power law (Eqn. 11) and the turbulence intensity profile follows Eqn. 12 [49] with a roughness height $z_0 = 1.8\times10^{-4}$ m.

214

215 After the successful formulation of the ABL flow, a 2:2:1 building model was established at
216 the position where the incident flow was measured. The windward façade was perpendicular
217 to the wind direction. The dimensions of the building model were 0.09 m in length and width,
218 and 0.045 m in height (H). Hot-wire measurements were conducted along nine vertical sample
219 lines around the building. The reattachment points on the roof (X_r) and behind the building
220 model (X_f) were also located by probing along the centerlines close to the wall. Fig. 3 provides
221 a schematic view of the measurements. The measurements around the building model were
222 repeated three times on different dates for the determination of the mean and variance of each
223 quantity.

All the measurements used a single-wire constant temperature anemometer (CTA) TSI IFA-300 mounted on a traverse system. The sampling frequency was 40 kHz, and for each measuring point, 2,097,152 samples were collected within one minute. The reference wind speed of U_H = 14.5 m/s ensured a building Reynolds number of $Re=U_H H/v$=43,500.

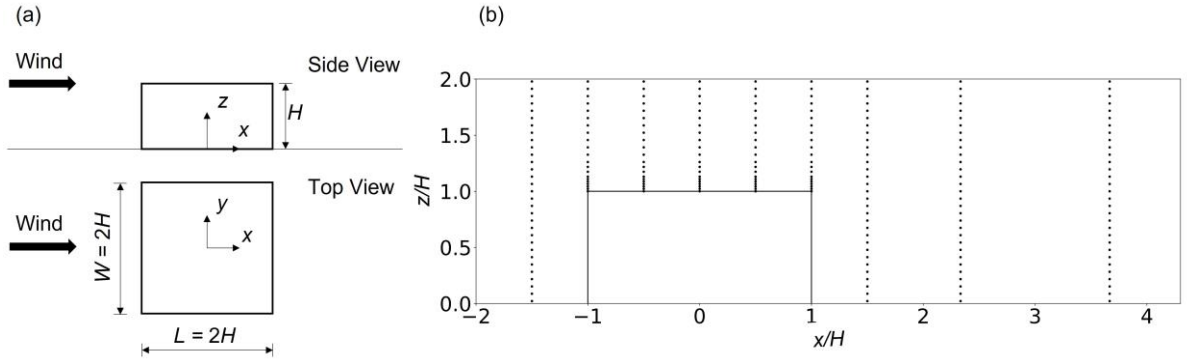

Figure 3 (a) Schematic of the wind tunnel experiment; (b) measurement locations. The streamwise velocity magnitude measured at these locations was for the calibrations based on point values (PD).

2.4 Validation metrics

The validity of the turbulence models needed to be quantitatively assessed with various metrics. This study employed the 'hit rate' value (*HR*) [50] and the so-called 'factor of two' value (*FAC2*) [51] for quantitative comparison between the point values of simulation results (SIM_i) and the experimental observation (EXP_i). Data points at which the model result differed from the observation value within an allowed range were marked as 'hits'. The allowable range was defined by a relative difference value (*RD*) and an absolute difference value (*AD*). The hit rate (*HR*) was defined as the fraction of the 'hits' out of all the data points and was calculated using the following equation:

$$HR = \frac{1}{n}\sum_{i=1}^{n} N_i \text{ with } N_i = \begin{cases} 1, \text{ if } \left|\frac{SIM_i - EXP_i}{EXP_i}\right| \le RD \text{ or } |SIM_i - EXP_i| \le AD \\ 0, \text{ else} \end{cases} \quad (13)$$

The $FAC2$ was similar to the HR because it also counted the fractions of marked data points, but the allowable difference was relaxed. In addition, data points with near-zero values were also counted if the model result and experimental observation were both within an allowable threshold (AD). The $FAC2$ was calculated using the following equation:

$$FAC2 = \frac{1}{n}\sum_{i=1}^{n} N_i \text{ with } N_i = \begin{cases} 1, \text{ if } 0.5 \le \left|\frac{SIM_i - EXP_i}{EXP_i}\right| \le 2 \\ 1, \text{ if } SIM_i \le AD \text{ and } EXP_i \le AD \\ 0, \text{ else} \end{cases} \quad (14)$$

The HR was chosen for the normalized velocity and normalized TKE, denoted HR_U and HR_k, respectively. For the normalized airborne contaminant concentration, the $FAC2$ was chosen and denoted $FAC2_C$, in light of the contrasting high and low values in the concentration field and the frequent appearance of near-zero values. The RD value was 0.25 for the normalized velocity and the normalized TKE. The AD values were 0.05, 0.017 [50], and 0.003 [51] for the normalized velocity, the normalized TKE, and the normalized contaminant concentration, respectively. An acceptable HR was defined as being no less than 66%, and an acceptable $FAC2_C$ as being no less than 50% [51].

In addition to the metrics for point values, the reattachment lengths on the roof (X_r) and behind the building (X_f) were evaluated for the single-building cases. The reattachment length prediction was deemed acceptable if it was within ±25% of the measured value.

3 Case setup

The previous section described the main calibration methods used in this study. For the calibration of model coefficients and the generalizability evaluations, appropriate configurations were required. This section describes the choice of test cases for generalizability evaluation, the details of the CFD simulations, and the setup of the EnKF.

3.1 Test cases

The wind tunnel experiment described in Subsection 2.3 provided the training data for the calibration process, and it is called the 'training case'. The generalizability evaluations required separate cases upon which the calibrations were not based (called 'test cases'). The test cases needed to be based on high-quality, comprehensive wind tunnel data for the velocity field, turbulence field, and concentration field, better with measurements of reattachment lengths. This investigation selected two test cases. Test case I was based on the benchmark case H provided by the Architectural Institute of Japan (AIJ) [52], a 1:1:2 shaped building model with a downwind release from a point source. Test case II was based on AIJ case K [52], point-source dispersion in a building array with a street canyon aspect ratio of unity. According to the classification by Oke [53], the configurations in the training case and test case I correspond to the 'isolated roughness flow' regime, featuring large-scale fluctuations and strong turbulence owing to the interaction between the building wake and the ABL. In comparison, the configuration of test case II corresponded to the skimming flow regime featuring a stable vortex and mild turbulence in each street canyon with little interference from the bulk. The test cases

279 could be used to test the generalizability of the model for the two distinctive flow types. This
280 section describes the two test cases briefly.
281 In test case I, the targeted building was that of AIJ case K, a 1:1:2 model with a height H = 0.2
282 m. The wind direction was perpendicular to the windward façade. The incident flow followed
283 the 0.25 power-law with a reference velocity at the building height U_H = 4.2 m/s. The flow
284 Reynolds number was 5.6×10^4. Tracer gas was released from a point source 0.25H downwind
285 of the leeward façade with a flow rate of $q = 5.83\times10^{-6}$ m^3/s. The concentration of the released
286 gas was $C_{gas}=1.0\times10^6$ ppm. A schematic of the experimental setup is shown in Fig. 4(a). Point
287 data for velocity (U), TKE (k), and tracer-gas concentration (C) was obtained on a vertical
288 plane in the middle (y = 0) and on multiple horizontal planes. The measured concentration C
289 was normalized by the reference concentration $C_0=C_{gas}q/(H^2U_H)$. Reattachment lengths on the
290 roof (X_r) and behind the building (X_f) were also measured. In test case I, the normalized
291 reattachment lengths (X_r/H and X_f/H) and point data for normalized velocity (U/U_H),
292 normalized TKE (k/U_H^2), and normalized concentration (C/C_0) in the y = 0 plane were used for
293 validation. Fig. 4(b) shows the 207 data points in the y = 0 plane.
294

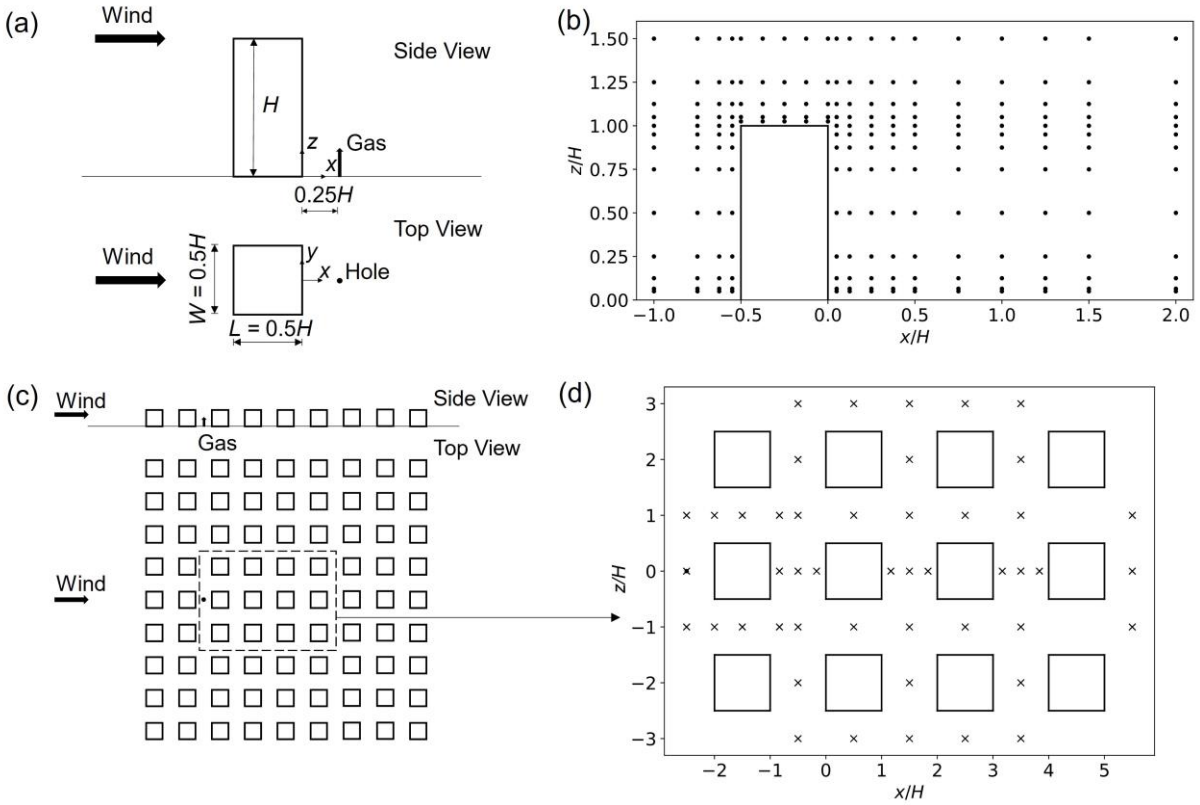

Figure 4 (a) Schematic and (b) measurement points of test case I; (c) schematic and (d) vertical sample line locations of test case II.

In test case II, the targeted building array was that of AIJ case K, represented by 9×9 cubic blocks with the same height H = 0.06 m and a uniform spacing equal to H. The wind direction was perpendicular to the windward façades. The incident flow had a reference velocity U_{ref} = 4.94 m/s at the reference height H_{ref} = 0.2 m. The Reynolds number defined by U_{ref} and H_{ref} was around 6.7×10^4. Tracer gas was released from a point source in the center of the second canyon with a flow rate of $q = 3.6\times10^{-6}$ m^3/s. The released gas had a concentration of $C_{gas}=1\times10^6$ ppm. Fig. 4(c) is a schematic of the experimental setup. Point data for velocity (U), TKE (k), and concentration (C) was obtained along vertical sample lines both in the canyons and on the streets with a total of 203 data points. Fig. 4(d) shows the top view of the sample

line locations. The measured concentration C was normalized by the reference concentration $C_0=C_{gas}q/(H_{ref}^2U_{ref})$. In Test case II, all the reported point values for normalized velocity (U/U_H), normalized TKE (k/U_H^2), and normalized concentration (C/C_0) were used for validation.

3.2 CFD simulation setups

As mentioned in Subsection 2.2, the EnKF calibration process required iterative CFD simulations of the training case. The calibrated coefficients were then used in the CFD simulations of the two test cases described in the subsection above for the generalizability evaluation. This subsection describes the computational domain, mesh generation, and numerical setups of the CFD simulations.

For the training case and for test case I, the computational domain was set in accordance with the AIJ guidelines [14]. The distances from the building to the inlet, the sides, and the top of the domain were all set as 5H, and the distance to the outlet was 10H. For test case II, the computational domain had the same setup as the wind tunnel experiment, since the building models were placed very close to the two sides of the wind tunnel, and the effect of the configuration on the airflow should be taken into consideration. The distances from the building array to the inlet, sides, top, and outlet boundary were 4H. 1.5H, 15.7H, and 10H, respectively. The outlines of the computational domains are shown in Fig. 5(a-c).

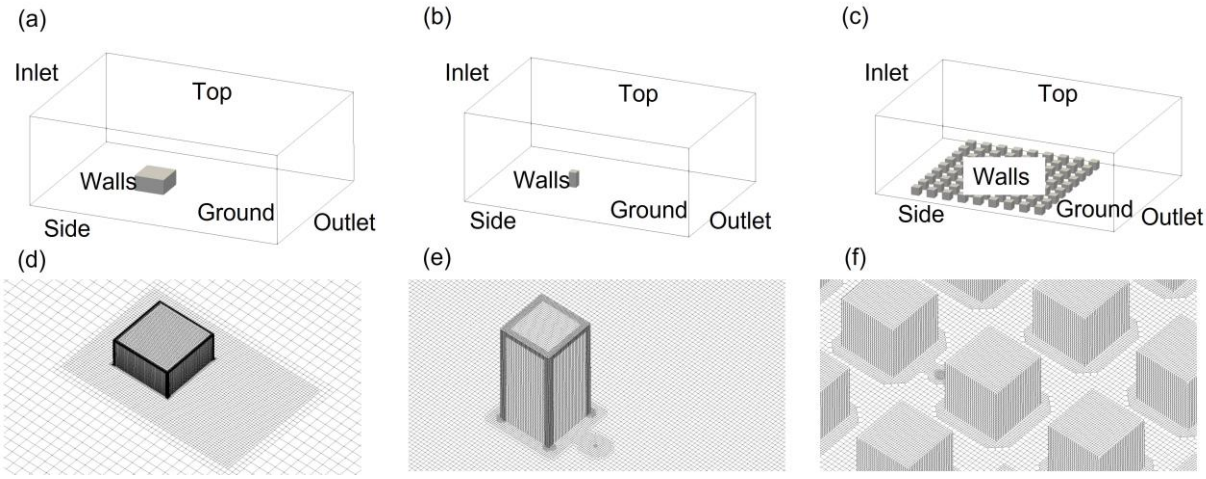

Figure 5 (a-c) Outline of the computational domain and (d-f) regional view of computational grids for the training case, test case I, and test case II.

Computational grids of the three cases were generated by the open-source mesh generation tool snappyHexMesh. Grid-independence studies (not shown here due to space limitations) were conducted to ensure the grid insensitivity of X_r, X_f, U, and k. In light of the computational cost of the calibration process, the mesh for the training case was as coarse as possible while ensuring grid insensitivity. For the two test cases, fine meshes were chosen to provide better resolution. The meshes employed for the training case and test cases I and II had cell numbers of 180,906, 1,420,509, and 2,055,383, respectively. The mesh details are shown in Fig. 5(d-f). Further refinements of the meshes contributed to an offset of X_r within 5% and offsets of X_f, HR_U, and HR_k within 2%.

The simulations were conducted in the open-source code OpenFOAM-v2012 [54]. The inlet boundary conditions for U and k were directly imposed by interpolating the measured profiles of the incident flow, while the inlet profile of ε was calculated from U and k using the empirical

equations suggested by Mochida et al. [36]. At the side and top boundaries, the symmetry boundary condition was applied. For the solid walls of the buildings, standard wall functions were applied for k, ε and ν_t, respectively, while for the ground surfaces, z_0-type wall functions suggested by Richards and Hoxey [31] were applied. The values of the surface roughness length z_0 in each case were estimated from the measured values of U and k closest to the ground in the incident flow [36]. In terms of physical properties, $\nu = 1.5\times10^{-5}$ was set for air and Sc = 0.7 for the passive scalar representing the ethylene used in the experiments. A standard value of 0.7 was used for Sc_t [21].

The simpleFoam solver based on the SIMPLE algorithm was employed to solve Eqs. (1-5), and then Eq. (6) was solved for the tracer-gas concentration field based on the steady-state results for the airflow field. The central linear scheme was applied for gradient terms and Laplacian terms. For the divergence terms, the second-order upwind scheme was used for U, the Van Leer scheme for k and ε, and the central linear scheme for C. The simulations were of second-order accuracy. The convergence criterion was 10^{-4} for the residuals of all the variables. An automatic post-processing script was used to obtain the reattachment lengths and point values of simulated results. The reattachment points were located by sampling along the streamwise centerlines on the roof and behind the building and finding the zero point for velocity.

3.3 Calibration setup

The discrepancy between the CFD results for the training case and the observation data from the wind tunnel experiment was imported to the EnKF for model coefficient calibration. This

subsection describes the setup of the EnKF. The initial ensemble of the coefficient set was generated using Halton sequence sampling [55] and ranged from 0.5 to 2.5 times the default values of the coefficients. Natural logarithms were taken for localization to ensure that the ensemble updates would not lead to negative values [56]. For example, in the calibration process for RKE, $\ln(\sigma_k)$, $\ln(\sigma_\varepsilon)$, $\ln(C_{\varepsilon 2})$ and $\ln(A_0)$ were worked upon. For each calibration, the input of the observation array $\boldsymbol{y}$ was constructed using the mean values of the measured quantities, while the observation covariance error $\boldsymbol{\Gamma}$ was built using the variances of the measured values from repeated experiments. The open-source code DAFI [57] was employed to perform the EnKF loop. The stopping criterion was that the change of each parameter was within 0.001.

As discussed in Section 1, the choice of the optimization objective is vital to the calibration process. In addition, the ensemble size used in ensemble methods can have a crucial effect on the results [58]. Before calibration of the six selected models that were introduced in Subsection 2.1, a preliminary test with respect to the choice of observation variables and ensemble sizes was conducted to determine the suitable calibration setup (see Subsection 4.1).

4 Results

As described in this section, a preliminary test was conducted to determine the observation and ensemble size for the main calibration. Next, the determined calibration setup was used to calibrate the six selected turbulence models with the wind tunnel data for the training case. Simulations of the training case and the two test cases were performed, using the original and

calibrated coefficients. Validation metrics of the model results were compared to assess the model performance.

4.1 Effects of chosen observations and ensemble sizes

As mentioned in Subsection 3.3, the proper choice of observations and ensemble sizes is vital to a successful calibration. This subsection presents the preliminary test with respect to the choice of optimization objectives and ensemble sizes. To minimize the uncertainty contributed by complex interconnections among the model coefficients and allow a clear comparison, RKE was chosen because it has the fewest model constants among the six models. Two observations were considered, namely, the point data (PD) and reattachment lengths (RL). Observation PD was constructed using a total of 229 values for the measured streamwise velocity magnitude $|U_x|$ in the wind tunnel experiment and observation RL was constructed using two values, X_r and X_f. The ensemble size should be determined from the number of model coefficients in each model. A rule of thumb is to choose an ensemble size no less than ten times the number of unknowns [59]. In this test, the selected ensemble sizes were 5, 10, and 20 times the number of unknowns; therefore, for RKE with four coefficients, ensemble sizes of 20, 40, 80 were chosen for comparison.

Six sets of RKE coefficients were obtained; they are compared with the original coefficients in Table 2. The coefficient sets were named in accordance with the chosen observations and ensemble sizes. For example, ‘PD20’ means a calibrated coefficient set for which the point data are the observation and the ensemble size is 20. Calibrations based on point data exhibited an irregular pattern as the ensemble size increased, while calibrations based on reattachment

399 lengths tended to converge. The calibration for RL20 failed because the ensemble size was
400 insufficient.
401
402 Table 2 Comparison of calibrated coefficient sets for Realizable k-ε model using different
403 EnKF settings. 'PD' means the calibrations were based on the point data and 'RL' the
404 reattachment lengths. The suffix numbers 20, 40, 80 mean the ensemble size employed in the
405 EnKF.

Coefficient Set	σ_k	σ_ε	$C_{\varepsilon 2}$	A_0
Original	1.0	1.2	1.9	4.0
PD20	0.79	0.71	0.96	0.24
PD40	1.36	0.06	6.60	0.84
PD80	1.00	1.60	1.50	4.4
RL20	-	-	-	-
RL40	1.50	0.21	2.60	0.68
RL80	1.59	0.33	2.15	0.69

406
407 The validation metrics for the training case using RKE with the obtained coefficients are
408 compared in Table 3. The original model exhibited a satisfactory hit rate but greatly
409 overpredicted both X_r and X_f. Among the calibrated models, PD40 had the highest hit rate, while
410 RL40 was the most accurate in reproducing the two reattachment lengths, with a slightly lower
411 hit rate than that when the original model was used. Models calibrated with 20 or 80 ensemble
412 members either failed to converge in the simulations or produced less satisfactory results.
413 Therefore, PD40 and RL40 were seen as representative for each corresponding optimization
414 objective and were further compared. Fig. 6 depicts the normalized streamwise velocity
415 magnitude distributions using the original model, PD40, and RL40 and compares them with
416 the measured values. The original and RL40 underpredicted the velocity overall, while PD40

417 delivered better agreement with the measured values, mainly in the wake region. However,

418 PD40 overpredicted the velocity on the roof.

419

420 Table 3 Comparison of normalized reattachment lengths (X_r/H and X_f/H) as well as hit rate for

421 velocity (HR_U) for the training case using Realizable k-ε with original and calibrated coefficient

422 sets for different EnKF settings.

Validation metrics	X_r/H (on the roof)		X_f/H (behind the building)		HR_U (%)
	Value	Offset (%)	Value	Offset (%)	
Original	0.49	+69.9	2.89	+88.15	82.54
PD20	0.12	-61.04	1.31	-14.71	75.11
PD40	0.32	+3.90	1.75	+13.93	85.59
PD80	-	-	-	-	-
RL20	-	-	-	-	-
RL40	0.31	+0.65	1.59	+3.52	81.66
RL80	0.33	+7.14	1.67	+8.72	79.91
Exp. (present study)	0.308		1.536		

423

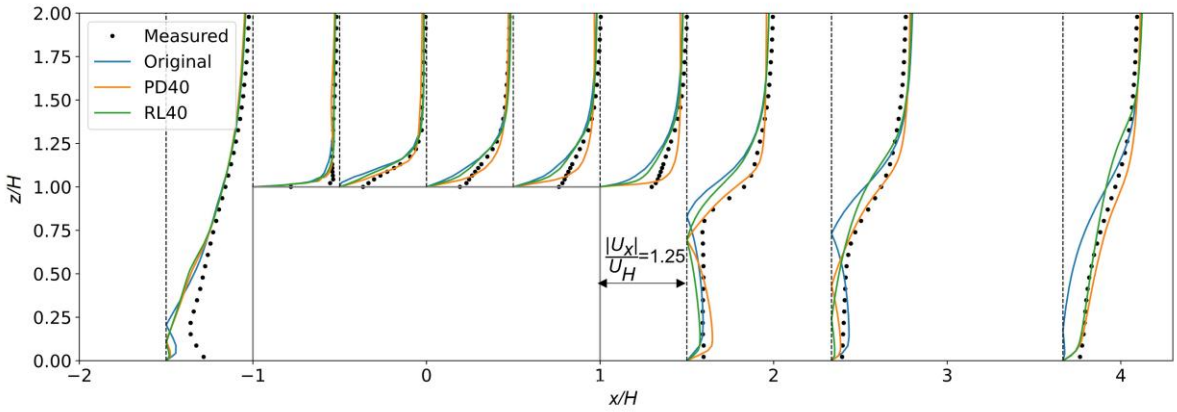

Figure 6 Vertical profiles of normalized streamwise velocity magnitude ($|U_x|/U_H$) in the vertical section y = 0 using three sets of RKE coefficients and measured experimentally, for the training case (2:2:1 building model). This comparison exhibits the effect of the optimization objectives.

424

425 According to the preliminary test, when the reattachment lengths were chosen as the

426 observation parameters, the EnKF successfully found the coefficient set that simultaneously

reproduced both X_r and X_f accurately. It is also apparent that for the RKE model, optimal reproduction of the reattachment lengths and the velocity field at the same time was not possible. Since an accurate reproduction of the recirculation zones is essential for predicting airborne pollutant transport, the reattachment lengths were prioritized and chosen as the optimization objective for the rest of the study. The ensemble size for each model was determined as ten times the number of unknowns since this size yielded a stable calibration process and produced reasonably good results.

4.2 Calibration of coefficients in selected turbulence models

With the EnKF setup as determined in the previous subsection, the chosen *k*-ε based models were calibrated. The coefficients for each model before and after the calibration are listed in Table 4. For clarity, the models with original coefficients are called 'original models' and have the suffix 'O'. Those with calibrated coefficients are called 'calibrated models' and have the suffix 'C'. Simulations of the training case using the original models and calibrated models were conducted. Table 5 shows the validation metrics of the results using different turbulence models before and after the calibration. None of the original models passed the validation in this case, since they all strongly overpredicted X_f by at least 50%. The original models also failed to reproduce X_r, with the exception of KLO. The HR_U values of the original models all exceeded the required minimum of 66%. After the calibration, the predictions of both X_r and X_f exhibited significant improvements for all the models. Before and after the calibration, HR_U was maintained at the same level for SKE, RKE, DKE, and KL, while improvements no less

than 10% were observed for RNG and MMK. All the calibrated models passed the validation, and thus the calibrations were successful.

Table 4 Original and calibrated coefficients in selected RANS-based turbulence models. The models with original coefficients were with the suffix 'O' and those with the calibrated coefficients were with the suffix 'C'. See Table 1 for the abbreviations for the turbulence models.

Model coefficients	C_μ	$C_{\varepsilon 1}$	$C_{\varepsilon 2}$	σ_k	σ_ε	A_0	α	β	η_0
SKEO	0.09	1.44	1.92	1.00	1.30	-	-	-	-
SKEC	0.04	3.31	6.42	1.98	0.70	-	-	-	-
RKEO	-	-	1.90	1.0	1.2	4.0	-	-	-
RKEC	-	-	2.6	1.50	0.21	0.68	-	-	-
RNGO	0.0845	1.42	1.68	0.71942	0.71942	-	-	0.012	4.38
RNGC	0.03	1.43	4.71	1.24	0.38	-	-	0.011	8.71
DKEO	0.09	1.44	1.92	1.00	1.30	-	1.00	-	-
DKEC	0.15	0.38	1.37	2.88	0.70	-	0.41	-	-
KLO	0.09	1.44	1.92	1.00	1.30	-	-	-	-
KLC	0.048	2.81	5.16	2.11	0.93	-	-	-	-
MMKO	0.09	1.44	1.92	1.00	1.30	-	-	-	-
MMKC	0.13	5.57	7.81	1.26	3.04	-	-	-	-

Table 5 Comparison of normalized reattachment lengths (X_r/H and X_f/H) and hit rate for velocity (HR_U) using different turbulence models for the training case (2:2:1 building model).

Validation metrics	Reattachment lengths				Point value
	X_r/H (on the roof)		X_f/H (behind the building)		HR_U (%)
	Value	Offset (%)	Value	Offset (%)	
SKEO	0.19	-38.31	2.32	+51.04	84.28
SKEC	0.27	-12.34	1.53	-0.39	85.15
RKEO	0.49	+59.09	2.89	+88.15	82.54
RKEC	0.31	+0.65	1.59	+3.52	81.66
RNGO	0.19	-38.31	2.30	+49.74	69.87
RNGC	0.31	+0.65	1.55	+0.91	83.84
DKEO	0.66	+114.29	2.43	+58.20	83.41
DKEC	0.33	+7.14	1.56	+1.56	80.35
KLO	0.36	+16.88	2.58	+67.97	82.96
KLC	0.34	+10.29	1.79	+16.54	82.53

MMKO	0.58	+88.31	2.60	+69.27	69.87
MMKC	0.35	+13.64	1.56	+1.56	82.10
Exp. (present study)	0.308	-	1.536	-	-

457 4.3 Test case I

458 To determine the generalizability of the calibrated models to a single building with a different
459 aspect ratio, simulations of test case I were conducted using the original and calibrated models.
460 Table 6 shows the validation metrics for this case. The original models greatly overpredicted
461 X_f, by at least 67.64% (DKEO) and up to 93.88% (RKEO). In addition, the original models
462 underpredicted X_r significantly, with the exception of RNGO, which predicted X_r exactly. Most
463 of the original models had reasonable HR_U. Still, none of the original models had an acceptable
464 HR_k, and the only original model that met the requirement for $FAC2_C$ was DKEO. In
465 comparison, the calibrated models all provided accurate predictions of X_f, with discrepancies
466 as low as 2.04% (RKEC and SKEC) and as high as 18.37% (MMKC), indicating a significant
467 improvement over the original models. However, in terms of X_r, most of the calibrated models
468 provided results that were only slightly better (SKEC, DKEC, and KLC) or that were even
469 worse (RKEC and RNGC). Only MMKC reproduced an adequate X_r that met the requirement.
470 HR_U remained at almost the same level before and after the calibration. HR_k exhibited
471 significant improvements for RKE, DKE, KL, and MMK but declined for SKE and RNG after
472 the calibration. Once again, the only model that met the requirement for HR_k was MMKC. With
473 respect to $FAC2_C$, the calibrated models exhibited considerable improvement over the original
474 models, with the exception of RKEC, and surpassed the required minimum. In the simulations
475 of test case I, the only model that passed the validation was MMKC.
476

Table 6 Comparison of normalized reattachment lengths (X_r/H and X_f/H), hit rates for velocity and turbulence kinetic energy (HR_U and HR_k) as well as the 'factor of two' value for concentration ($FAC2_C$) using different turbulence models for test case I (1:1:2 building model).

Validation metrics	Reattachment lengths				Point value		
	X_r/H (on the roof)		X_f/H (behind the building)		HR_U (%)	HR_k (%)	$FAC2_C$ (%)
	Value	Offset (%)	Value	Offset (%)			
SKEO	0.09	-66.17	1.17	+70.55	68.12	33.33	47.83
SKEC	0.17	-36.09	0.7	+2.04	70.53	32.37	61.35
RKEO	0.08	-69.92	1.33	+93.88	61.35	28.5	24.15
RKEC	0.03	-88.72	0.7	+2.04	70.05	56.52	29.95
RNGO	0.26	-2.26	1.23	+79.30	70.05	42.51	45.89
RNGC	0.19	-28.57	0.81	+18.08	72.95	33.33	55.56
DKEO	0.15	-43.61	1.15	+67.64	69.57	39.62	50.72
DKEC	0.18	-32.33	0.63	-8.16	73.91	42.02	61.35
KLO	0.16	-39.85	1.26	+83.67	68.12	38.16	46.38
KLC	0.16	-39.85	0.77	+12.24	71.98	50.24	61.35
MMKO	0.1	-62.41	1.17	+70.55	70.04	43.96	47.34
MMKC	0.22	-17.29	0.56	-18.37	71.5	68.12	62.32
Exp.	0.266	-	0.686	-	-	-	-

Fig. 7 to 9 compared the contours and vertical profiles at the chosen locations of the normalized velocity, normalized TKE, and normalized concentration in the vertical plane $y = 0$ using SKE and MMK with original and calibrated coefficients with the experimental data. These two models were chosen because SKE is the basic formulation of the k-ε model, while MMKC was the only model that passed the validation for test case I, since it was the only model that met the requirement both for X_r and HR_k.

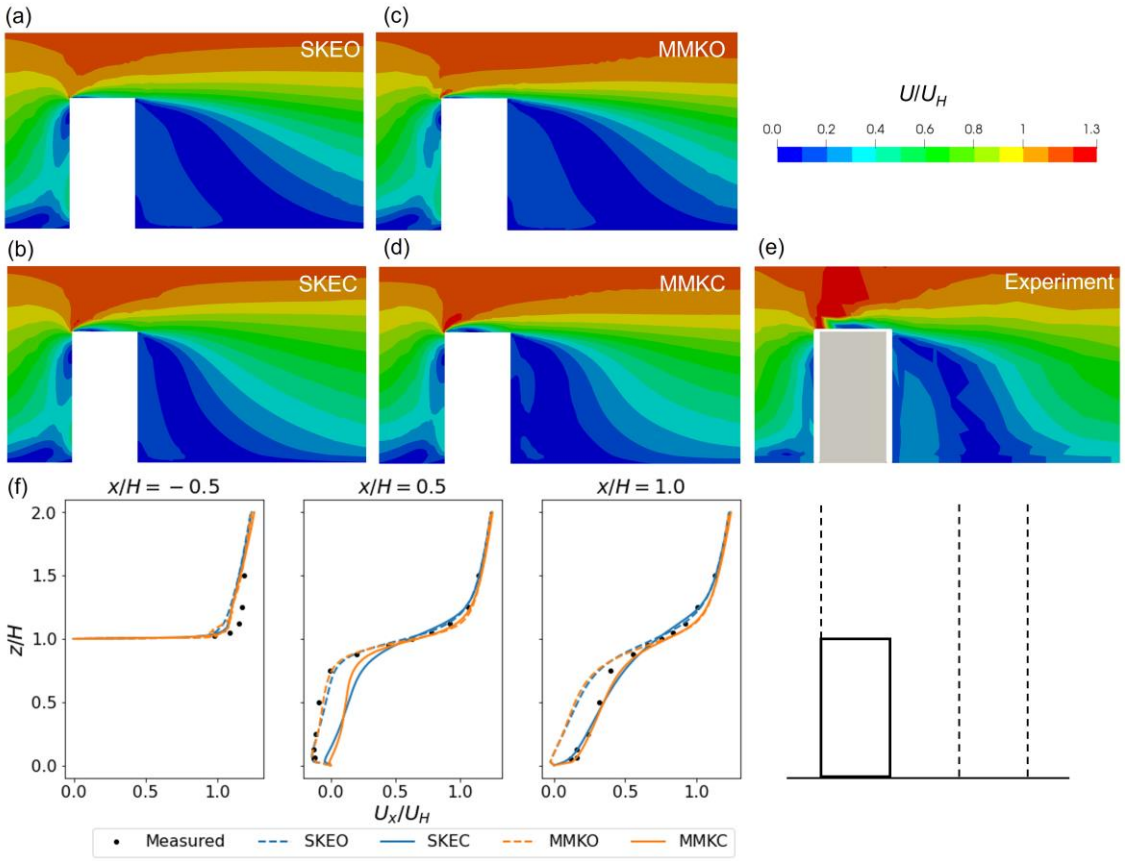

Figure 7 Contours of normalized velocity magnitude (U/U_H) using (a) SKEO, (b) SKEC, (c) MMKO, (d) MMKC, (e) determined experimentally (remade from the database [52]), and (f) vertical profiles of normalized streamwise velocity, in the vertical plane $y = 0$ for test case I (1:1:2 building model).

488

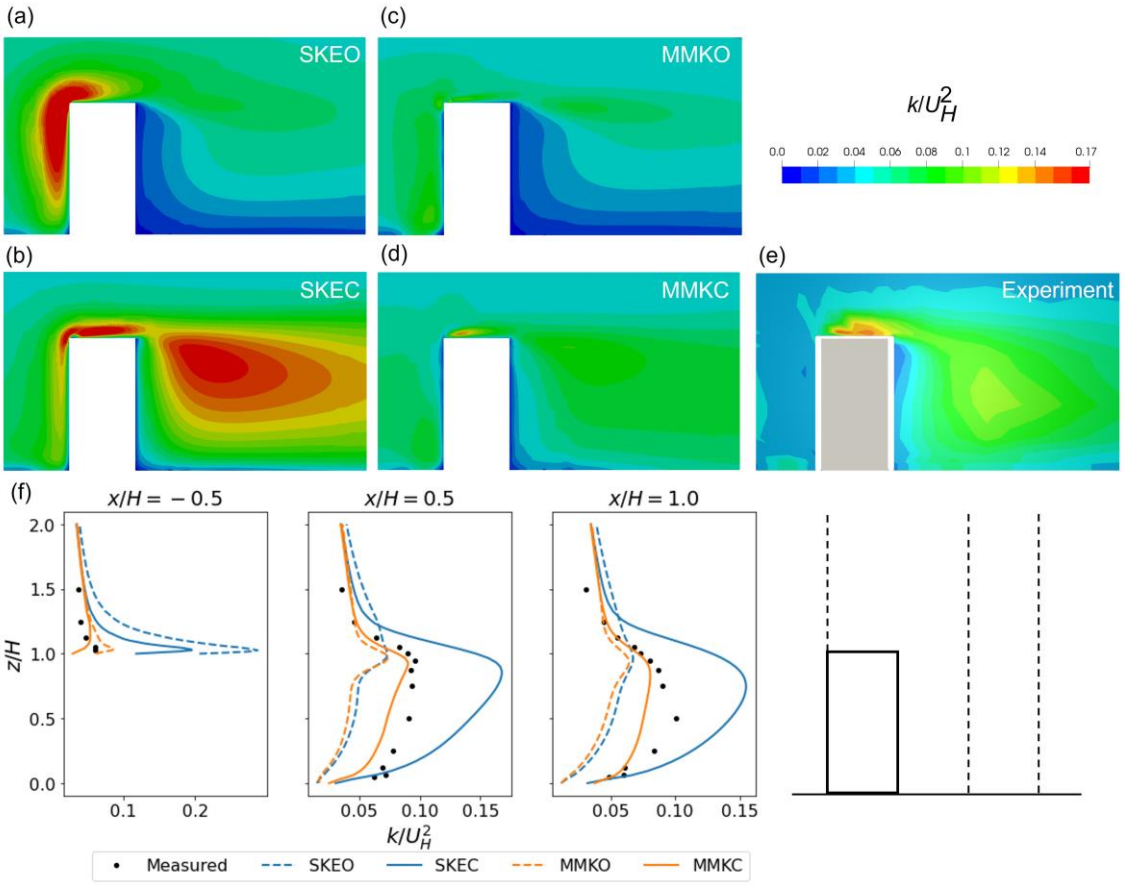

Figure 8 Contours of normalized turbulence kinetic energy (k/U_H^2) using (a) SKEO, (b) SKEC, (c) MMKO, (d) MMKC, (e) determined experimentally (remade from the database [52]), and (f) vertical profiles of normalized turbulence kinetic energy, in the vertical plane $y = 0$ for test case I (1:1:2 building model).

489

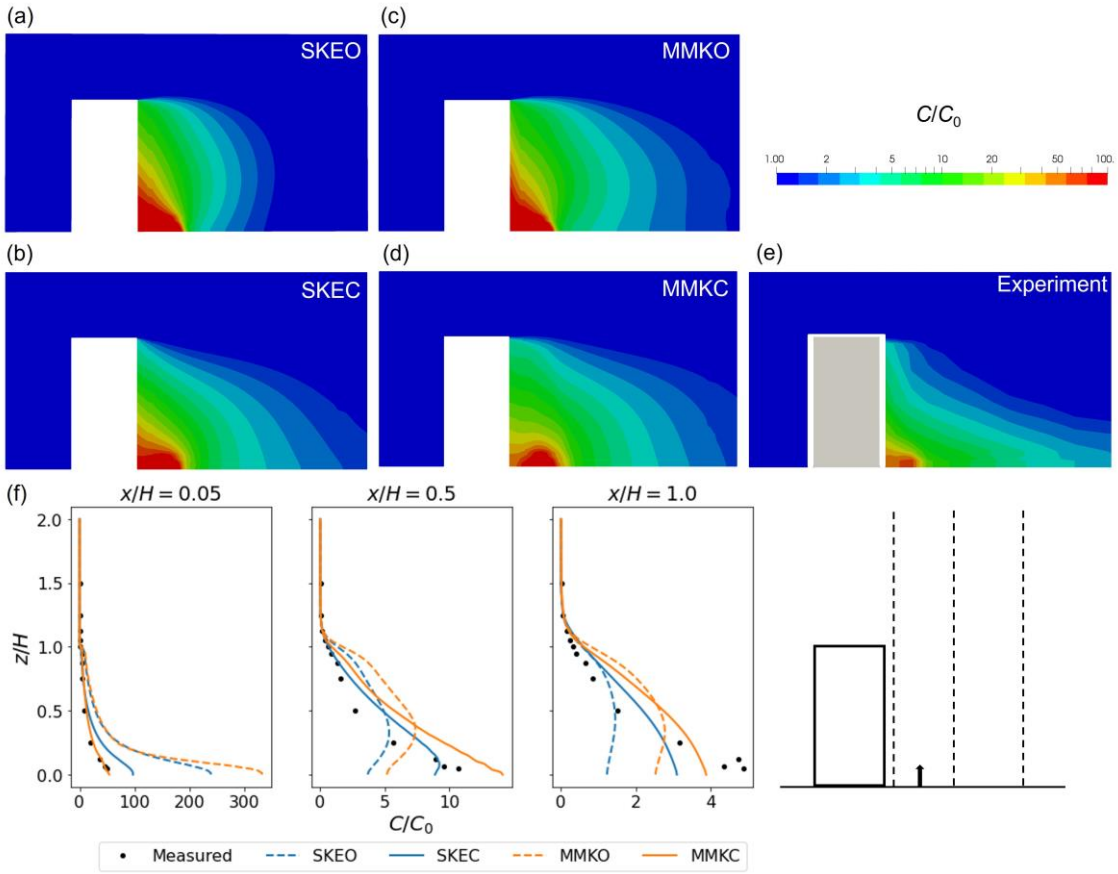

Figure 9 Contours of normalized tracer-gas concentration (C/C_0) using (a) SKEO, (b) SKEC, (c) MMKO, (d) MMKC, (e) determined experimentally (remade from the database [52]), and (f) vertical profiles of normalized tracer-gas concentration, in the vertical plane $y = 0$ for test case I (1:1:2 building model).

As shown in Fig. 7, the distributions of the simulated velocity using SKEO and MMKO were very similar, and a similarity was also observed among all the original models (not shown). Furthermore, all the calibrated models predicted the velocity field with slight differences. The results of the original models differed from those of the calibrated models mainly in the recirculation regions, which can be more clearly identified in the verticle profiles of the streamwise velocity as shown in Fig. 7(f). The accurate prediction of the reattachment length behind the building by the calibrated models contributed to the better agreement with the

498 measured streamwise velocity in the far-wake of the building, for example, at x/H = 1.0.
499 However, the improvement was not global. For example, at x/H = 0.5 in the near-wake,
500 decreased accuracy was observed for the calibrated models.
501 Unlike the observed pattern in the velocity field, the distributions of TKE differed significantly
502 among the models, as depicted in Fig. 8. SKEO greatly overpredicted the TKE in the
503 impingement region of the windward wall, where there was only a slight overprediction by
504 MMKO. Neither SKEO nor MMKO reproduced the peak value of TKE above the central area
505 of the roof. The distributions of TKE behind the building predicted by SKEO and MMKO were
506 very similar, both with apparent underprediction. After the calibration, the overprediction of
507 TKE in front of the windward wall by both models was mitigated, but the overprediction by
508 SKEC was still extreme. The spread of the overpredicted TKE from the upwind corner to the
509 roof by SKEC was greater than that by SKEO. The overprediction was transported further
510 downstream to the wake region, where an enormously exaggerated TKE can be observed for
511 SKEC. The overprediction of TKE on the roof and in the building wake was also observed for
512 other calibrated models (not shown), with the exception of MMKC, which reproduced a
513 distribution of TKE on the roof and behind the building that agreed well with the experimental
514 data.
515 For the tracer-gas concentration field shown in Figure 9, differences in the results for different
516 models were observed mainly near the gas source, near the leeward wall, and in the far region
517 of the wake. All the models overpredicted the concentration near the gas source. The
518 overprediction was transported upward, and thus an over-contaminated leeward wall was

519 predicted by SKEO and MMKO. The overprediction of concentration at the leeward wall was
520 mitigated for SKEC and MMKC, with MMKC predicting a vertical concentration distribution
521 near the leeward façade that agreed well with the experimental results (x/H = 0.05). The passive
522 scalar was not accurately transported downstream by SKEO and MMKO (x/H = 0.5, 1.0). In
523 comparison, the ground-level concentration distribution reproduced by SKEC and MMKC was
524 in better agreement with the experimental data. However, none of the turbulence models
525 reported the concentration distribution in the upper region of the wake as it was observed in
526 the experiment. All the models overpredicted the concentration in this region.

527 4.4 Test case II

528 For evaluation of the generalizability of the calibrated models to a building array, simulations
529 of test case II were conducted using the original and calibrated models. Table 6 lists the
530 validation metrics for this case. Most of the original models predicted turbulence and tracer-
531 gas concentration fields that agreed well with the experimental data. However, none of the
532 original models met the requirement for HR_U, and thus they did not pass the validation for case
533 II. In comparison, most of the calibrated models were more accurate in reproducing the airflow
534 field and concentration field. The highest HR_U and $FAC2_C$ were both achieved by MMKC.
535 However, all the models predicted the TKE less accurately after the calibration. The calibrated
536 models that passed the validation were SKEC, DKEC, and MMKC, among which MMKC had
537 the highest HR_U, HR_k, and $FAC2_C$.
538

Table 7 Comparison of hit rates for velocity and turbulence kinetic energy (HR_U and HR_k) as well as the 'factor of two' value for concentration ($FAC2_C$) using different turbulence models for test case II (building array).

Validation metrics	HR_U (%)	HR_k (%)	$FAC2_C$ (%)
SKEO	62.07	84.23	64.53
SKEC	85.71	67.98	70.44
RKEO	46.31	83.25	68.97
RKEC	39.90	81.77	71.43
RNGO	53.69	80.30	63.55
RNGC	69.46	66.01	42.36
DKEO	63.05	84.24	64.53
DKEC	84.23	80.78	62.56
KLO	63.05	84.23	65.51
KLC	89.16	58.12	71.92
MMKO	62.56	83.25	66.50
MMKC	90.64	67.98	83.74

The normalized scalar velocity, normalized TKE, and normalized concentration in the canyons downwind of the release point (y = 0) using SKE and MMK with original and calibrated coefficients are compared with experimental data in Fig. 10. Figs. 11 to 13 compare the contours of the quantities in the same plane using MMK with original and calibrated coefficients. The velocity distributions in the canyons predicted by the four turbulence models were very similar (Fig. 10(a)), all agreeing well with the experimental values, especially at ground level. MMKC predicted a decreased velocity level compared to MMKO, near the leeward façade of the downwind building and therefore a different vortex structure (Fig. 11). The TKE predictions differed greatly between the original and calibrated models, as shown in Fig. 10(b). The original models reproduced the TKE distribution quite well. In contrast, the calibrated models predicted only the TKE at ground level with acceptable accuracy and overpredicted the TKE in the upper regions. Fig. 12 illustrates a higher level of TKE for

MMKC not only in the canyon but also in the bulk stream and the impingement region of the leeward building. When it came to the gas dispersion in the canyons (Fig. 10(c)), all the models overpredicted the concentration level at the location where the gas was released (x = -2.5H). The measured normalized concentration had a global peak value of 205.68 only in the proximity of the source. Both the original and calibrated MMK strongly overpredicted the concentration in the canyon where the gas was released, as shown in Fig. 13. An over-contaminated leeward wall of the upwind building was predicted by MMKO, while MMKC mitigated the overprediction, similar to the observation in test case I as illustrated in Fig. 9. In the first (x = -0.5H) and second (x = 1.5H) canyons downwind of the source, the original models overpredicted the concentration level, while the calibrated models achieved better results. In the third (x = 3.5H) and forth (x = 5.5H) canyons, all four models predicted the concentration distribution accurately.

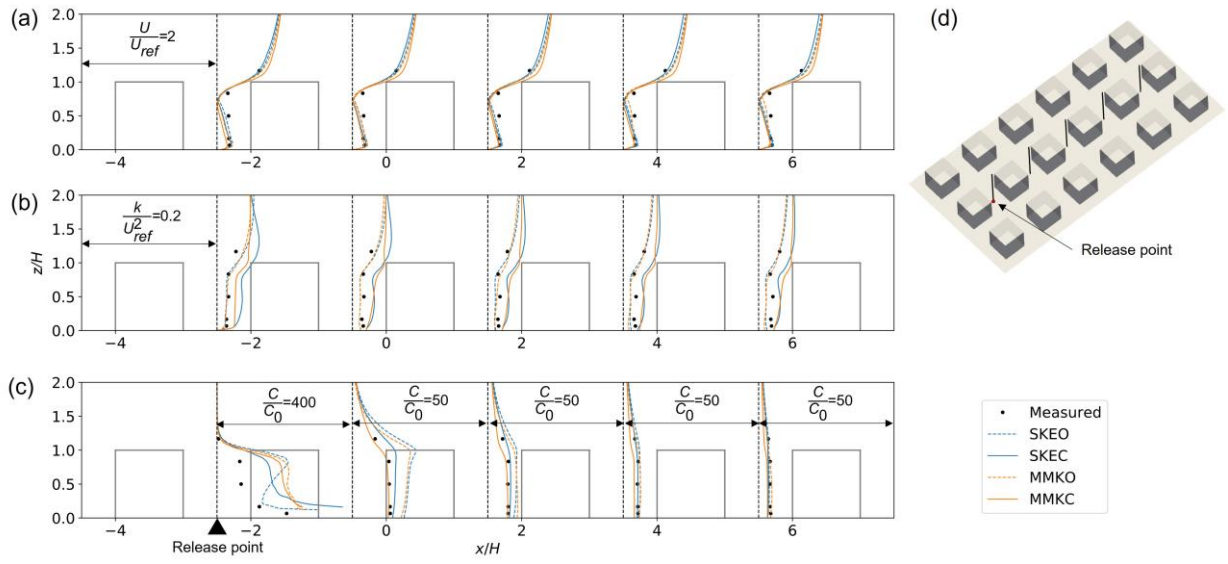

Figure 10 Vertical profiles of (a) normalized velocity magnitude (U/U_{ref}), (b) normalized turbulence kinetic energy (k/U_{ref}^2), and (c) normalized concentration (C/C_0) in (d) the vertical lines in the canyons downwind of the source (y = 0), for test case II (building array).

568

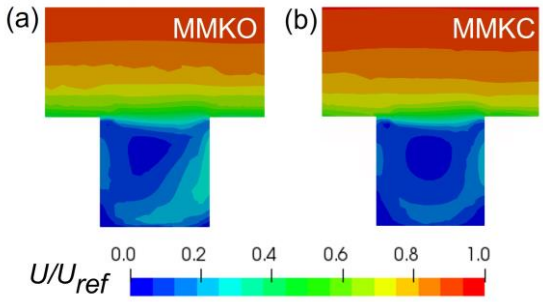

Figure 11 Contours of normalized velocity magnitude (U/U_{ref}) in the y = 0 vertical plane using (a) MMKO and (b) MMKC, in the canyon where the gas was released, for test case II (building array).

569

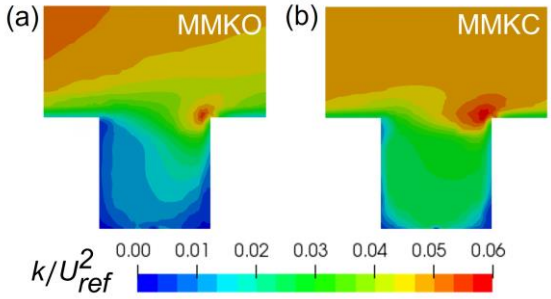

Figure 12 Contours of normalized turbulence kinetic energy (k/U_{ref}^2) in the y = 0 vertical plane using (a) MMKO and (b) MMKC, in the canyon where the gas was released, for test case II (building array).

570

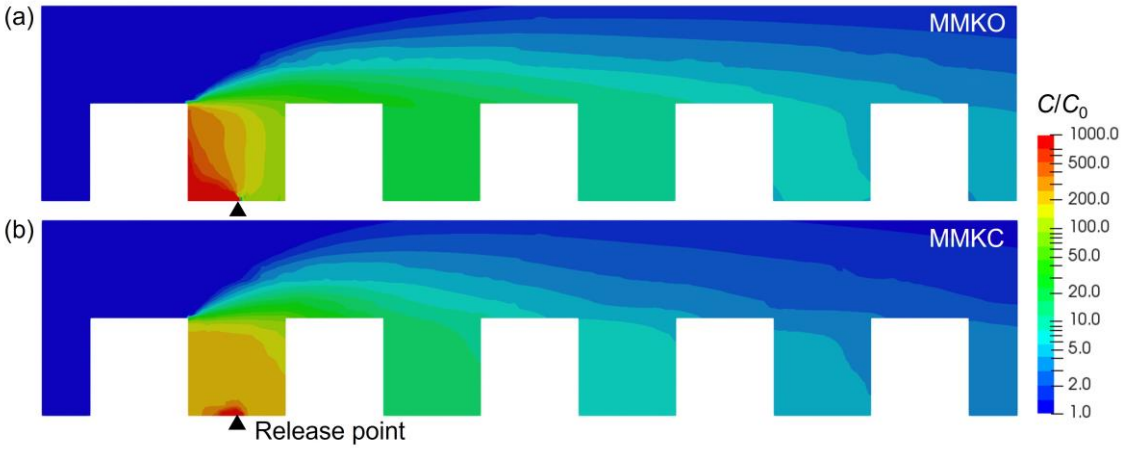

Figure 13 Contours of normalized concentration (C/C_0) in the y = 0 vertical plane using (a) MMKO and (b) MMKC, in the canyons downwind of the source, for test case II (building array).

571

572 **5 Discussion**

573 In the preliminary test for the appropriate EnKF calibration setup, the calibrated coefficients
574 based on velocity point data exhibited an irregular pattern as the ensemble size increased. In
575 contrast, the calibrated coefficients based on the reattachment lengths tended to be independent
576 of the ensemble size. The possible reasons are as follows. As pointed out in previous studies,
577 the two-equation models have inherent shortcomings [25,27,28]. They cannot be forced to
578 achieve a perfect match with the whole dataset simply by tuning the model coefficients. As a
579 result, the prediction accuracy of different quantities at different locations can be conflicting,
580 making the EnKF optimizer unstable or even diverge. It is stable to choose only a single
581 quantity like the streamwise velocity magnitude for point-data-based calibration. Moreover, in
582 this study, there were uncertainties in the point data for the streamwise velocity magnitude
583 measured by the single-wire CTA, especially in the low-velocity regions. The single wire CTA

584 measures the ‘mean magnitude’ of the streamwise velocity, while SRANS predicts the
585 ‘magnitude of mean’. The mismatch in the low-velocity regions could have been considered in
586 the calibration process by relaxing $\boldsymbol{\Gamma}$ in Eqn. 10 for improved stability. However, this handling
587 would not necessarily contribute to better results. Models calibrated against point data in
588 Shirzadi et al. [27] and Shirzadi et al. [28] still overpredicted X_f by around 30% in their training
589 case. In contrast, the optimization objective of reattachment lengths is straightforward and
590 easier to meet. It is reasonable to prioritize the accurate prediction of reattachment lengths,
591 since they are key features of the airflow, and the velocity field cannot be perfectly reproduced
592 with either observation setup.
593 The generalization from the training case (2:2:1 isolated building) to test case I (1:1:2 isolated
594 building) was successful only for MMKC. It is indicated that the calibration of model
595 coefficients is meaningful for generalizability only when the turbulence model is suitable for
596 the problem in a formulation sense. In the wake region, although all the calibrated models
597 accurately predicted X_f in test case I, most of them exaggerated the TKE behind the building,
598 except for MMKC. In terms of the impingement region, most of the calibrated models could
599 not predict X_r as accurately in test case I as in the training case. The generalizability concerning
600 X_r is challenging since X_r is not only related to the building aspect ratio, but also the inflow and
601 predicted turbulence level at the building height. MMK has a well-formulated production
602 limiter, which takes effect not only in the upwind impingement region but also in the lower
603 part of the recirculation region behind the building where $\Omega/S < 1$ [41]. In comparison, KL has
604 the flaw of inconsistency between the modeling of P_k and the Reynolds stress [41], and the

limiter of DKE takes effect only in the upwind impingement region [60]. Results in this study seem to suggest that MMKC is the only model that exhibits strong potential for generalizability to other single-building problems. The performance can be hardly achieved by the original two-equation models. The generalization to test case II seems a bigger leap, in light of the pitfall contributed by distinctive flow features [23]. For single building problems, the large-scale unsteady motions in the wake of the building cannot be resolved by SRANS, which is the main reason that SRANS underpredicted TKE in the wake and overpredicted X_f [61]. The calibrated models compensate for, often with exaggerations of, the underpredicted TKE to achieve an accurate X_f. However, the compensation for the single-building isolated roughness flow is not compatible with the street canyon skimming flow, since the large-scale flow structures are not dominant and the turbulence should be stabilized by the steady vortex in the canyon. Urban airflow comprises combinations of isolated flow, wake-interference flow, and skimming flow [53]. It is understandable that in Shirzadi et al. [28], calibrations for the same model based on different urban problems such as wind around a single building, street canyon flow, and cross-ventilation produced distinctive coefficient sets. The incompatibility issue requires further modifications to the model formulations for a seamless adaption, accompanied by coefficient calibrations. The comprehensiveness of the measured data in the two test cases facilitated the awareness of the several generalizability issues. However, one limitation of the chosen test cases is that the simplified geometries cannot fully represent real urban topologies. Future works will test the model performance in real urban domains after addressing the challenging incompatibility issues.

In previous studies, sensitivity analysis concerning one single coefficient can help to analyze the contribution of the tuning [27,29,33]. However, for the change of the whole set of coefficients, it is difficult to analyze the mechanism since the effects of the multiple coefficients are interconnected. Common patterns of the coefficient change cannot be directly identified (Table 4). Multi-parameter sensitive analysis may provide additional information. The dispersion modeling in this study employed the standard Sc_t value of 0.7. Previous studies tended to use smaller values of Sc_t for urban dispersion problems to compensate for the underprediction of TKE by RANS-based turbulence models [21]. This compensation approach cannot be generalized and may lead to misleading results in different cases. A change of Sc_t value from the standard one can only ensure improved accuracy at limited positions while leading to worse results at the rest regions [62]. So the standard value was used in the present study and no sensitivity analysis concerning Sc_t was conducted. However, since the Sc_t value should not be global, more advanced Sc_t formulations may yield better results [63,64]. Furthermore, steady RANS cannot reproduce the fluctuation of flow properties, which is vital for the accurate prediction of airborne pollutant dispersion [65]. Transient simulations such as unsteady RANS may provide better results. Whether the calibrated model constants for steady RANS can be readily applied to transient simulations requires further investigation.

6 Conclusions

In this study, the EnKF approach was adopted to calibrate turbulence model coefficients for urban problems. To optimize the accuracy and generalizability of the obtained model, both the

effects of optimization objectives and the turbulence model formulations were especially considered. The conclusions are as follows:

With proper setup with respect to ensemble sizes and optimization objectives, the EnKF approach can be successfully employed in the calibration of turbulence model coefficients for urban problems. An ensemble size 10 times the number of model coefficients was sufficient for a stable calibration. Prioritizing the key features of airflow in the observation setup can further improve the reconstruction of experimental data, exhibiting greater effectiveness than commonly employed point-data-based approaches for coefficient calibration.

The generalizability of the calibrated turbulence models is closely related to their formulations. The generalization within the isolated roughness flow regime can be realized, provided that the model formulation is suitable. For a single-building test case with a different aspect ratio, different calibrated models exhibited distinctive generalizability. All the calibrated models maintained the accuracy of the reattachment length behind the building (X_f), but they often predicted an exaggerated TKE in the building wake. Furthermore, most of the models exhibited poor generalizability when it came to the reattachment on the roof (X_r). The only model that provided an acceptable prediction of X_r and TKE was MMKC, which was also the most accurate in predicting tracer-gas concentration in this case.

A distinctive flow regime can also lead to generalizability issues. In the building-array test case, all the calibrated models overpredicted TKE, except in the ground-level regions. The generalizability of the models calibrated against a single-building case is believed to be limited for multi-building problems, despite the fact that most of the calibrated models yielded

improved results for velocity and tracer-gas concentration in the building-array simulation. The generalization from the isolated roughness flow regime to the skimming flow regime requires further modifications to the model formulation.

The turbulence model finally identified by this study is MMKC, which exhibits strong potential for generalizability to single-building problems. Future studies should focus on modifying the model formulation to make it generalizable across a broader range of urban problems, taking complex building topology and different urban airflow regimes into consideration. In addition, the applicability of the calibrated coefficients for transient simulations should be investigated.

Acknowledgements

This study was partially supported by the National Natural Science Foundation of China (NSFC) through grant No. 52108084, and by the China Postdoctoral Science Foundation through Grant No. 2020M680886.

References

[1] Y. Zhang, Z. Gu, C.W. Yu, Review on numerical simulation of airflow and pollutant dispersion in urban street canyons under natural background wind condition, Aerosol Air Qual. Res. 18 (2018) 780–789. doi:10.4209/aaqr.2017.09.0303.

[2] B. Blocken, T. Stathopoulos, J. Carmeliet, J.L.M. Hensen, Application of computational fluid dynamics in building performance simulation for the outdoor

688 environment: An overview, J. Build. Perform. Simul. 4 (2011) 157–184.
689 doi:10.1080/19401493.2010.513740.
690 [3] A. Gupta, T. Stathopoulos, P. Saathoff, Wind tunnel investigation of the downwash
691 effect of a rooftop structure on plume dispersion, Atmos. Environ. 46 (2012) 496–507.
692 doi:10.1016/j.atmosenv.2011.08.039.
693 [4] T. Stathopoulos, L. Lazure, P. Saathoff, A. Gupta, The effect of stack height, stack
694 location and rooftop structures on air intake contamination: a laboratory and full-scale
695 study, IRSST, 2004.
696 [5] J. Zou, Y. Yu, J. Liu, J. Niu, K. Chauhan, C. Lei, Field measurement of the urban
697 pedestrian level wind turbulence, Build. Environ. 194 (2021) 107713.
698 doi:10.1016/j.buildenv.2021.107713.
699 [6] N. Antoniou, H. Montazeri, M. Neophytou, B. Blocken, CFD simulation of urban
700 microclimate: Validation using high-resolution field measurements, Sci. Total
701 Environ. 695 (2019). doi:10.1016/j.scitotenv.2019.133743.
702 [7] S. Liu, W. Pan, X. Zhao, H. Zhang, X. Cheng, Z. Long, Q. Chen, Influence of
703 surrounding buildings on wind flow around a building predicted by CFD simulations,
704 Build. Environ. 140 (2018) 1–10. doi:10.1016/j.buildenv.2018.05.011.
705 [8] B. Blocken, T. Stathopoulos, J.P.A.J. van Beeck, Pedestrian-level wind conditions
706 around buildings: Review of wind-tunnel and CFD techniques and their accuracy for
707 wind comfort assessment, Build. Environ. 100 (2016) 50–81.
708 doi:10.1016/j.buildenv.2016.02.004.

709 [9] B. Blocken, Computational Fluid Dynamics for urban physics: Importance, scales,
710 possibilities, limitations and ten tips and tricks towards accurate and reliable
711 simulations, Build. Environ. 91 (2015) 219–245. doi:10.1016/j.buildenv.2015.02.015.
712 [10] B. Blocken, LES over RANS in building simulation for outdoor and indoor
713 applications: A foregone conclusion?, Build. Simul. 11 (2018) 821–870.
714 doi:10.1007/s12273-018-0459-3.
715 [11] P.A. Mirzaei, CFD modeling of micro and urban climates: Problems to be solved in
716 the new decade, Sustain. Cities Soc. 69 (2021) 102839. doi:10.1016/j.scs.2021.102839.
717 [12] B. Blocken, 50 years of Computational Wind Engineering: Past, present and future, J.
718 Wind Eng. Ind. Aerodyn. 129 (2014) 69–102. doi:10.1016/j.jweia.2014.03.008.
719 [13] J. Franke, A. Hellsten, K.H. Schlünzen, B. Carissimo, The COST 732 Best Practice
720 Guideline for CFD simulation of flows in the urban environment: A summary, Int. J.
721 Environ. Pollut. 44 (2011) 419–427. doi:10.1504/IJEP.2011.038443.
722 [14] Y. Tominaga, A. Mochida, R. Yoshie, H. Kataoka, T. Nozu, M. Yoshikawa, T.
723 Shirasawa, AIJ guidelines for practical applications of CFD to pedestrian wind
724 environment around buildings, J. Wind Eng. Ind. Aerodyn. 96 (2008) 1749–1761.
725 doi:10.1016/j.jweia.2008.02.058.
726 [15] B. Blocken, W.D. Janssen, T. van Hooff, CFD simulation for pedestrian wind comfort
727 and wind safety in urban areas: General decision framework and case study for the
728 Eindhoven University campus, Environ. Model. Softw. 30 (2012) 15–34.
729 doi:10.1016/j.envsoft.2011.11.009.

730 [16] B. Blocken, C. Gualtieri, Ten iterative steps for model development and evaluation
731 applied to Computational Fluid Dynamics for Environmental Fluid Mechanics,
732 Environ. Model. Softw. 33 (2012) 1–22. doi:10.1016/j.envsoft.2012.02.001.
733 [17] R. Yoshie, A. Mochida, Y. Tominaga, H. Kataoka, K. Harimoto, T. Nozu, T.
734 Shirasawa, Cooperative project for CFD prediction of pedestrian wind environment in
735 the Architectural Institute of Japan, J. Wind Eng. Ind. Aerodyn. 95 (2007) 1551–1578.
736 doi:10.1016/j.jweia.2007.02.023.
737 [18] Y. Tominaga, T. Stathopoulos, Numerical simulation of dispersion around an isolated
738 cubic building: Model evaluation of RANS and LES, Build. Environ. 45 (2010) 2231–
739 2239. doi:10.1016/j.buildenv.2010.04.004.
740 [19] S. Vardoulakis, R. Dimitrova, K. Richards, D. Hamlyn, G. Camilleri, M. Weeks, J.F.
741 Sini, R. Britter, C. Borrego, M. Schatzmann, N. Moussiopoulos, Numerical Model
742 Inter-comparison for Wind Flow and Turbulence Around Single-Block Buildings,
743 Environ. Model. Assess. 16 (2011) 169–181. doi:10.1007/s10666-010-9236-0.
744 [20] P. Gousseau, B. Blocken, G.J.F. van Heijst, CFD simulation of pollutant dispersion
745 around isolated buildings: On the role of convective and turbulent mass fluxes in the
746 prediction accuracy, J. Hazard. Mater. 194 (2011) 422–434.
747 doi:10.1016/j.jhazmat.2011.08.008.
748 [21] Y. Tominaga, T. Stathopoulos, Turbulent Schmidt numbers for CFD analysis with
749 various types of flowfield, Atmos. Environ. 41 (2007) 8091–8099.
750 doi:10.1016/j.atmosenv.2007.06.054.

751 [22] H. Xiao, P. Cinnella, Quantification of model uncertainty in RANS simulations: A
752 review, Prog. Aerosp. Sci. 108 (2019) 1–31. doi:10.1016/j.paerosci.2018.10.001.
753 [23] J.L. Wu, J.X. Wang, H. Xiao, A Bayesian Calibration–Prediction Method for
754 Reducing Model-Form Uncertainties with Application in RANS Simulations, Flow,
755 Turbul. Combust. 97 (2016) 761–786. doi:10.1007/s10494-016-9725-6.
756 [24] N. Glover, S. Guillas, L. Malki-Epshtein, Statistical calibration of CFD modelling for
757 street canyon flows, Proc. Build. Simul. 2011 12th Conf. Int. Build. Perform. Simul.
758 Assoc. (2011) 1513–1520.
759 [25] S. Guillas, N. Glover, L. Malki-Epshtein, Bayesian calibration of the constants of the
760 k-ε turbulence model for a CFD model of street canyon flow, Comput. Methods Appl.
761 Mech. Eng. 279 (2014) 536–553. doi:10.1016/j.cma.2014.06.008.
762 [26] Q.M. Zahid Iqbal, A.L.S. Chan, Pedestrian level wind environment assessment around
763 group of high-rise cross-shaped buildings: Effect of building shape, separation and
764 orientation, Build. Environ. 101 (2016) 45–63. doi:10.1016/j.buildenv.2016.02.015.
765 [27] M. Shirzadi, P.A. Mirzaei, M. Naghashzadegan, Improvement of k-epsilon turbulence
766 model for CFD simulation of atmospheric boundary layer around a high-rise building
767 using stochastic optimization and Monte Carlo Sampling technique, J. Wind Eng. Ind.
768 Aerodyn. 171 (2017) 366–379. doi:10.1016/j.jweia.2017.10.005.
769 [28] M. Shirzadi, P.A. Mirzaei, Y. Tominaga, RANS model calibration using stochastic
770 optimization for accuracy improvement of urban airflow CFD modeling, J. Build. Eng.
771 32 (2020) 101756. doi:10.1016/j.jobe.2020.101756.

772 [29] F. Toja-Silva, C. Peralta, O. Lopez-Garcia, J. Navarro, I. Cruz, Roof region dependent
773 wind potential assessment with different RANS turbulence models, J. Wind Eng. Ind.
774 Aerodyn. 142 (2015) 258–271. doi:10.1016/j.jweia.2015.04.012.
775 [30] J.M. Gimenez, F. Bre, Optimization of RANS turbulence models using genetic
776 algorithms to improve the prediction of wind pressure coefficients on low-rise
777 buildings, J. Wind Eng. Ind. Aerodyn. 193 (2019) 103978.
778 doi:10.1016/j.jweia.2019.103978.
779 [31] P.J. Richards, R.P. Hoxey, Appropriate boundary conditions for computational wind
780 engineering models using the k-ε turbulence model, Comput. Wind Eng. 47 (1993)
781 145–153. doi:10.1016/B978-0-444-81688-7.50018-8.
782 [32] H. Kato, S. Obayashi, Approach for uncertainty of turbulence modeling based on data
783 assimilation technique, Comput. Fluids. 85 (2013) 2–7.
784 doi:10.1016/j.compfluid.2012.09.002.
785 [33] H. Kato, K. Ishiko, A. Yoshizawa, Optimization of parameter values in the turbulence
786 model aided by data assimilation, AIAA J. 54 (2016) 1512–1523.
787 doi:10.2514/1.J054109.
788 [34] M. Yang, Z. Xiao, Parameter uncertainty quantification for a four-equation transition
789 model using a data assimilation approach, Renew. Energy. 158 (2020) 215–226.
790 doi:10.1016/j.renene.2020.05.139.
791 [35] Y. Toparlar, B. Blocken, B. Maiheu, G.J.F. van Heijst, A review on the CFD analysis
792 of urban microclimate, Renew. Sustain. Energy Rev. 80 (2017) 1613–1640.

793 doi:10.1016/j.rser.2017.05.248.
794 [36] A. Mochida, Y. Tominaga, S. Murakami, R. Yoshie, T. Ishihara, R. Ooka, Comparison
795 of various k-ε models and DSM applied to flow around a high-rise building - Report
796 on AIJ cooperative project for CFD prediction of wind environment, Wind Struct. An
797 Int. J. 5 (2002) 227–244. doi:10.12989/was.2002.5.2_3_4.227.
798 [37] D.C. Wilcox, Turbulence modeling for CFD, DCW industries La Canada, CA, 1998.
799 [38] S. Murakami, Overview of turbulence models applied in CWE–1997, J. Wind Eng.
800 Ind. Aerodyn. 74–76 (1998) 1–24. doi:10.1016/S0167-6105(98)00004-X.
801 [39] B.E. Launder, D.B. Spalding, The numerical computation of turbulent flows, Comput.
802 Methods Appl. Mech. Eng. 3 (1974) 269–289. doi:10.1016/0045-7825(74)90029-2.
803 [40] M. Kato, B.E. Launder, The modelling of turbulent flow around stationary and
804 vibrating cylinders, in: Ninth Symp. Turbul. Shear Flows, 1993.
805 [41] M. Tsuchiya, S. Murakami, A. Mochida, K. Kondo, Y. Ishida, Development of a new
806 k-ε model for flow and pressure fields around bluff body, J. Wind Eng. Ind. Aerodyn.
807 67–68 (1997) 169–182. doi:10.1016/S0167-6105(97)00071-8.
808 [42] P.A.A. Durbin, On the k-3 stagnation point anomaly, Int. J. Heat Fluid Flow. 17 (1996)
809 89–90. doi:10.1016/0142-727X(95)00073-Y.
810 [43] T.-H.H. Shih, W.W. Liou, A. Shabbir, Z. Yang, J. Zhu, A new k-ϵ eddy viscosity
811 model for high reynolds number turbulent flows, Comput. Fluids. 24 (1995) 227–238.
812 doi:10.1016/0045-7930(94)00032-T.
813 [44] V. Yakhot, S.A. Orszag, S. Thangam, T.B. Gatski, C.G. Speziale, Development of

814 turbulence models for shear flows by a double expansion technique, Phys. Fluids A. 4
815 (1992) 1510–1520. doi:10.1063/1.858424.
816 [45] G. Evensen, Sequential data assimilation with a nonlinear quasi-geostrophic model
817 using Monte Carlo methods to forecast error statistics, J. Geophys. Res. 99 (1994).
818 doi:10.1029/94jc00572.
819 [46] M.A. Iglesias, K.J.H. Law, A.M. Stuart, Ensemble Kalman methods for inverse
820 problems, Inverse Probl. 29 (2013) 045001. doi:10.1088/0266-5611/29/4/045001.
821 [47] H.P.A.H. Irwin, Design and use of spires for natural wind simulation, Natl.
822 Aeranautical Establ. Lab. Tech. Rep. (1979).
823 [48] I.-B. Lee, C. Kang, S. Lee, G. Kim, J. Heo, S. Sase, Development of vertical wind and
824 turbulence profiles of wind tunnel boundary layers, Trans. ASAE. 47 (2004) 1717–
825 1726. doi:10.13031/2013.17614.
826 [49] American Society of Civil Engineers, Wind tunnel studies of buildings and structures,
827 American Society of civil engineers, 1999.
828 [50] J.L. Santiago, A. Martilli, F. Martín, CFD simulation of airflow over a regular array of
829 cubes. Part I: Three-dimensional simulation of the flow and validation with wind-
830 tunnel measurements, Boundary-Layer Meteorol. 122 (2007) 609–634.
831 doi:10.1007/s10546-006-9123-z.
832 [51] M. Schatzmann, H. Olesen, J. Franke, COST 732 model evaluation case studies:
833 approach and results, 2010.
834 [52] Architectural Institute of Japan, Guidebook for CFD predictions of urban wind

environment, (2008). https://www.aij.or.jp/jpn/publish/cfdguide/index_e.htm (accessed September 11, 2021).

[53] T.R. Oke, Street design and urban canopy layer climate, Energy Build. 11 (1988) 103–113. doi:10.1016/0378-7788(88)90026-6.

[54] OpenCFD Ltd., OpenCFD Release OpenFOAM® v2012, (2020). https://www.openfoam.com/news/main-news/openfoam-v20-12 (accessed September 11, 2021).

[55] J.H. Halton, Algorithm 247: Radical-inverse quasi-random point sequence, Commun. ACM. 7 (1964) 701–702.

[56] M. Conjard, H. Omre, Data assimilation in spatio-temporal models with non-Gaussian initial states-The selection ensemble Kalman model, Appl. Sci. 10 (2020). doi:10.3390/APP10175742.

[57] C.A.M. Ströfer, X.-L. Zhang, H. Xiao, DAFI: An Open-Source Framework for Ensemble-Based Data Assimilation and Field Inversion, Commun. Comput. Phys. 29 (2021) 1583–1622. doi:10.4208/cicp.OA-2020-0178.

[58] M.A. Iglesias, A regularizing iterative ensemble Kalman method for PDE-constrained inverse problems, Inverse Probl. 32 (2016) 25002. doi:10.1088/0266-5611/32/2/025002.

[59] X. He, F. Zhao, M. Vahdati, Uncertainty quantification of spalart-allmaras turbulence model coefficients for compressor stall, Proc. ASME Turbo Expo. 2C-2020 (2020) 1–18. doi:10.1115/GT2020-15014.

856 [60] Y. Tominaga, A. Mochida, S. Murakami, S. Sawaki, Comparison of performance of
857 various revised k-ε models applied to CFD analysis of flowfield around a high-rise
858 building, J. Archit. Plan. (Transactions AIJ). 67 (2002) 47–54.
859 doi:10.3130/aija.67.47_2.
860 [61] Y. Tominaga, Flow around a high-rise building using steady and unsteady RANS
861 CFD: Effect of large-scale fluctuations on the velocity statistics, J. Wind Eng. Ind.
862 Aerodyn. 142 (2015) 93–103. doi:10.1016/j.jweia.2015.03.013.
863 [62] C. Lin, R. Ooka, H. Kikumoto, T. Sato, M. Arai, CFD simulations on high-buoyancy
864 gas dispersion in the wake of an isolated cubic building using steady RANS model and
865 LES, Build. Environ. 188 (2021) 107478. doi:10.1016/j.buildenv.2020.107478.
866 [63] T. Lauriks, R. Longo, D. Baetens, M. Derudi, A. Parente, A. Bellemans, J. van Beeck,
867 S. Denys, Application of Improved CFD Modeling for Prediction and Mitigation of
868 Traffic-Related Air Pollution Hotspots in a Realistic Urban Street, Atmos. Environ.
869 246 (2021) 118127. doi:10.1016/j.atmosenv.2020.118127.
870 [64] C. Lin, R. Ooka, H. Kikumoto, H. Jia, Eulerian RANS simulations of near-field
871 pollutant dispersion around buildings using concentration diffusivity limiter with travel
872 time, Build. Environ. 202 (2021) 108047. doi:10.1016/j.buildenv.2021.108047.
873 [65] Y. Tominaga, T. Stathopoulos, Steady and unsteady RANS simulations of pollutant
874 dispersion around isolated cubical buildings: Effect of large-scale fluctuations on the
875 concentration field, J. Wind Eng. Ind. Aerodyn. 165 (2017) 23–33.
876 doi:10.1016/j.jweia.2017.02.001.

877